

Capillary bridge: Transition from equilibrium to hydrodynamic state

B. Radoev^a, I.T. Ivanov^{a,*}, P. Petkov^b

^a Dept. of Physical Chemistry, University of Sofia, "St. Kliment Ohridski", J. Bourchier 1, Sofia, Bulgaria

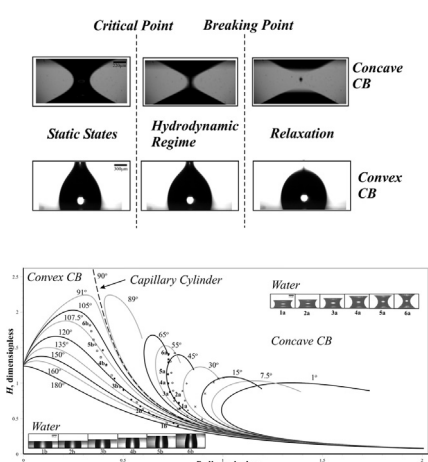
^b Dept. of Chemical Engineering, University of Sofia, "St. Kliment Ohridski", J. Bourchier 1, Sofia, Bulgaria



HIGHLIGHTS

- Theoretical analysis of CB critical points and its comparison with experimental data.
- Experimental study of the transition from equilibrium to dynamic CB states.
- Modelling the hydrodynamics and breakage process of CB.

GRAPHICAL ABSTRACT



ARTICLE INFO

Article history:

Received 4 November 2015

Received in revised form 15 January 2016

Accepted 21 January 2016

Available online 29 January 2016

Keywords:

Capillary bridge

Critical point

Instability

Hydrodynamics

ABSTRACT

The present study is focused on the capillary bridge (CB) behaviour in the vicinity of its critical state. As known, a critical state is an extreme, unstable point, by crossing which a given system passes from one state to another. In our case, this passage is from equilibrium (static) to a hydrodynamic state. The hydrodynamic process, called here hydrodynamic regime occurring in concave CB is characterized by local deformations in the region of its neck, registered via a high speed camera (~1000 fps). The information obtained from the experiment is interpreted on the basis of a lubrication model. The theoretical evaluations correlate satisfactorily with the experimental data.

© 2016 Elsevier B.V. All rights reserved.

1. Introduction

As with many classical subjects, there is a big difference in the knowledge of capillary bridge (CB) equilibrium (static) and

non-equilibrium (dynamic) states. For static CB, there is a well-studied theoretical approach, based on Young-Laplace's equation [1,2] which comes with solutions of a broad spectrum [3]. The situation with the dynamics of CB is much more complicated and the reasons for that are well-known. Firstly, in respect to dynamics, there is a great diversity of situations and effects. For example, the rheology can be separated into two distinct phases: bulk (3D) and surface (2D). Furthermore, in bulk rheology there are some specific

* Corresponding author.

E-mail address: fhi@chem.uni-sofia.bg (I.T. Ivanov).

effects of the so-called three-phase contact (TPC) zone, like slip-page [4–7] and its alternative molecular model [8,9]. The important Marangoni effect on surface hydrodynamics is basically not studied at all for reasons of the difficulties with the TPC rheology. The studies of Marangoni stresses in evaporating sessile droplets can be given as an exception in this respect [10–13].

The transitions from static to dynamic states are an interesting part of the CB behaviour. The most expressive examples of these transitions are near the unstable points of a system. The stability of an equilibrium state is a subject of the theoretical mechanics and its analysis follows the respective classical methods [14,15]. In a former paper of ours [16], special considerations were made about a particular region near the boundary of the CB equilibrium states. Beyond this boundary the considered system cannot exist in an equilibrium state any more, which gives ground for all of its parameters to be considered as critical. Among them, the most expressive one is the critical bridge thickness, H_{cr} . In the cited paper it is pointed out [16], that a given CB (at constant contact angle) could be pressed unlimited (formally to zero thickness, $H \rightarrow 0$) but it shows limitation at stretching. In other words, equilibrium thicknesses are closed in the range $0 \leq H \leq H_{\text{cr}}$, where H_{cr} (critical thickness) is the upper limit of the solution of Young–Laplace equation with certain boundary conditions. The most popular example for restricted stretching is the catenoid, for which it is shown that $H_{\text{cr}} = 0.66R$ [17], where R is the contact radius. In Fig. 5 can be seen a family of theoretical curves, calculated for certain contact angles and thus named isogons. They show well defined maxima identical with the critical thicknesses, i.e. $H_{\text{max}} \equiv H_{\text{cr}}$. (see Appendix A).

The present study is devoted to situations shortly before and after the critical point.

2. Materials and methods

2.1. Experimental setup

Our experimental setup consists of a micrometre, onto the measuring arms of which two square ($20 \times 20 \times 2$ mm) stainless steel supporting plates were fixed, parallel to one another. Two 22×22 mm microscope cover glasses (ISOLAB) of soda lime silica composition, glued to the supporting plates, were selected as working surfaces. Images were recorded by using a high speed camera, MotionXtra N3, which was mounted onto a horizontal optical tube with appropriate magnification.

The light system was designed for the bundle of light to be directed perpendicularly to the electronic sensor of a high speed camera and, at the same time, the waist of the photographed CB to appear exactly in the middle position in the light bundle (Fig. 1).

2.2. Solid surface preparation

Hydrophilic glass surfaces were pre-cleaned with 99.9% $\text{C}_2\text{H}_5\text{OH}$ and washed with deionized (Millipore) water before being glued to the supporting plates.

Hydrophobized glass cover slides have been used for the convex CB formation. The preliminary hydrophobization was done

with PDMS (Rhodia Silicones, 47V1000), following a certain procedure [18]. Before gluing the slides, they were washed with 99.9% $\text{C}_2\text{H}_5\text{OH}$.

2.3. Materials

All experiments were carried out with deionized (Millipore) water or room-temperature ionic liquids (RTIL). RTIL are salts in liquid states and were chosen mainly because they exhibit very low vapour pressure (10^{-10} Pa at 25°C), i.e. no volume changes take place during the experiment. Three RTIL were used for CB formation between hydrophilic glass surfaces. Summary of their physical parameters is presented in Table 1 and their ions structural formula is given in Fig. 2 [19].

2.4. Static measurements

A small droplet of $\approx 1\text{ mm}^3$ volume, is placed in the middle of the lower glass slide. The upper glass slide is moved towards the droplet until a capillary bridge is formed. The formed CB is stretched/pressed in small steps ($\Delta H \sim 0.1\text{ mm}$). After each step, the system is given time to relax and it is recorded as a profile image (see Fig. 3). The stretching continues until the critical thickness is reached. The experiment is repeated several times. Concerning the effects due to evaporation, the direct volume decrease plays no role, since the theoretical relations are in scaled (volume invariant) form (Appendix A). The droplet volume is specially chosen in order to be able to neglect the effect of gravitational deformation. As known the criterion for neglecting these effects is the droplet linear sizes to be smaller than the so-called capillary length $(\sigma/\rho g)^{1/2}$, which in our case is of order of 1 mm.

2.5. Dynamic measurements

After an unstable/critical point (H_u/H_{cr}) is reached, the system passes into the next stage, called here hydrodynamic regime. The given snapshots (Fig. 3) show typical CB brakeage evolution stages. These brakeage patterns are not unique. It is observed with other capillary shapes such as pendant droplets (drop-weight method [20]), jets [21,22], etc.

In hydrodynamic regime concave CBs undergo spontaneous deformation, thinning and breakage in the neck region, which appears to be the system's weakest region. In the case of convex CBs, the deformation occurs in a quite different place. As seen from Fig. 3, breakage occurs near the upper plate, in the region where inflection point takes place [16] but, for the lack of definitive experimental proof, this remains only a hypothesis for now. Note that with the start of the hydrodynamic regime, the stretching is ceased ($\Delta H = 0$), proving that deformation processes have a spontaneous character, rather than driven by external forces. The occurrence of thinning is due to instabilities and the thus arisen capillary pressure difference. The whole process takes up to a few milliseconds ending with breakage. The non-equilibrium (hydrodynamic) state capturing acquires high-speed (>1000 fps) camera. After the breakage, the system passes into the final stage, named here relaxation. During the relaxation, the two big parts (drops) of the broken bridge retract, forming pendant/sessile droplets at the upper/lower plates. While breaking one up to several small droplets form, which, due to gravity and inertial moments, merge with one or both of the big drops (Fig. 3).

2.6. Image analysis

The collected images of both "static" and "dynamic" measurements are subjected to image analysis, which consist of three essential steps: capturing the CB image, detection of CB profile

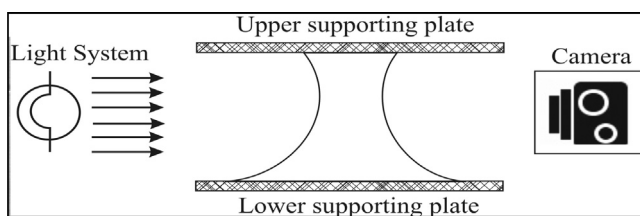
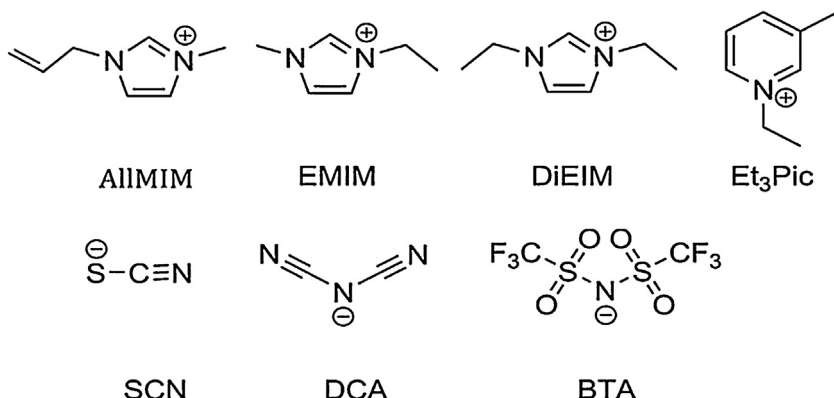
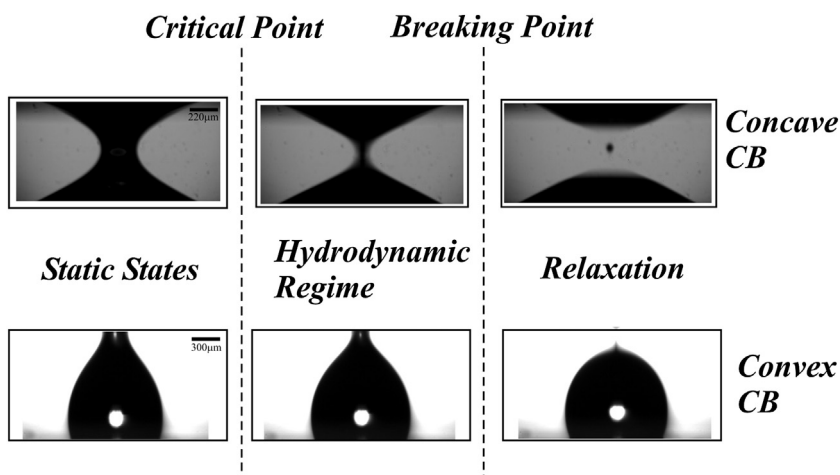


Fig. 1. Schematic representation of the experimental setup.

Table 1

Physical parameters of the used liquids.

Sample	Ionic liquid		Surface tension, σ [mN/m]	Density, ρ [kg/m ³]	Viscosity, μ [mPa s]	σ/μ [m/s]
	Cation	Anion				
IL 1	AllIM	DCA	37.6 ± 0.07	1071	16	2.35
IL 5	DiEMIM	BTA	31.6 ± 0.03	1450	27.9	1.133
IL 6	Et ₃ Pic	BTA	32.9 ± 0.04	1512	36.6	0.899
Water			72.3 ± 0.08	998	0.98	73.776

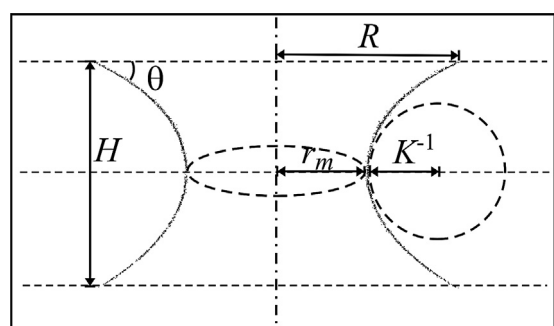
**Fig. 2.** Structural formula of ionic liquid ions.**Fig. 3.** Selected CB images of static, hydrodynamic and relaxation states. Note the drastic differences between concave and convex CB forms.

edge and statistical approximation (fitting) of the determined profile [23]. The fitting of the CB profile gives us the opportunity to calculate its meridional curvature, K , but is perhaps the most questionable step of the whole image analysis. It is well-known that the exact solution of the CB profile is elliptic curves of different kinds (nodoid, unduloid, etc. [2]). For our study, however, the exact solution is not needed, because we are concerned only with the narrow neck region. This gives us the right to approximate the exact curve by a second order polynomial (parabola) around its maximum without losing accuracy (Fig. 4). As for the other geometrical parameters: thickness (H), contact angle (θ) and the neck and contact radii (r_m, R), they are measured directly.

3. Results and discussion

3.1. Static states

The static states, as already mentioned, are equilibrium (mechanical) states defined in the region of thicknesses, $0 \leq H \leq H_{cr}$.

**Fig. 4.** Measurable geometrical parameters. H —bridge thickness; R —contact radius; K^{-1} —meridional curvature radius; r_m —azymuthal curvature radius; θ —contact angle.

Their properties and characteristics follow from the solution of Young-Laplace equation at given boundary conditions. As far as static CB have been already analyzed elsewhere [see e.g. in Ref.

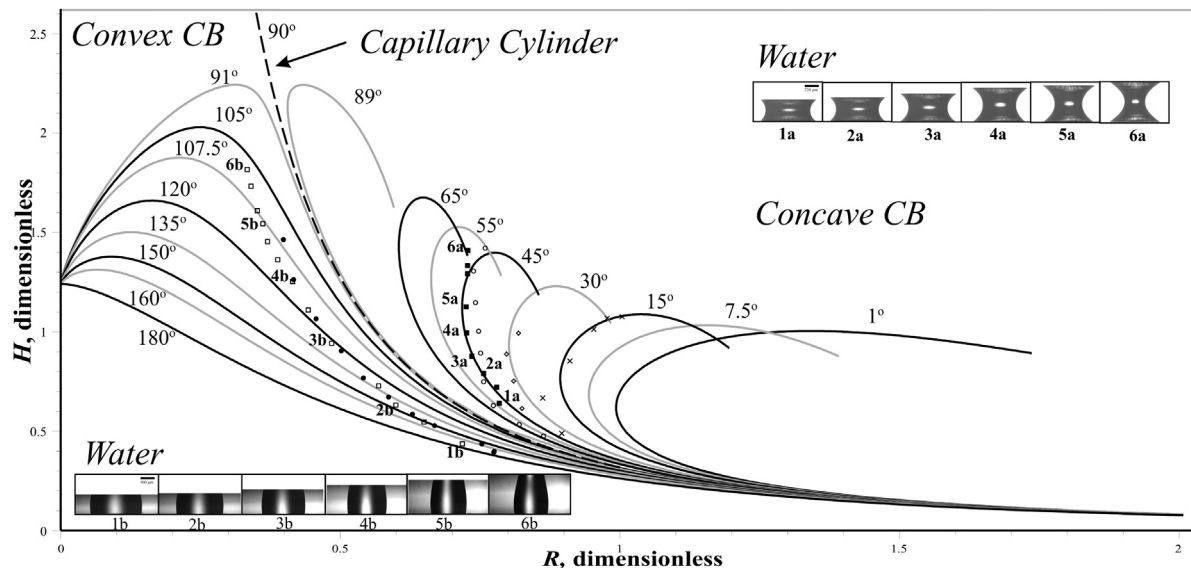


Fig. 5. Diagram of bridge thickness (H) vs. contact radius (R). Solid lines—*theoretical isogones*; circle—*experimental data for IL_1*; box, solid box and solid circle—*experimental data for water*; diamond—*experimental data for IL_6*; diagonal cross—*experimental data for IL_5*. The photo series illustrate the real CB shape deformation at stretching.

[16]], here are summarized only the important results of the present study (Figs. 5 and 6), combined with some more details in Appendix A.

Here again we stress the fact that H_{\max} and H_{cr} (Fig. 5) are identical, i.e. above this maximum the considered system cannot exist in an equilibrium state any more. Another important fact is that the experimental data are located only on the one side (branch) of the graphics with respect to H_{\max} : for concave CBs—left branch, but for convex CB—right branch. The two branches of $H(R)$ are typical as the solution of the Young-Laplace equation is double valued [see e.g. in Refs. [16,24]]. Both solutions represent mechanical equilibrium states, but they are thermodynamically non-equivalent and the experimental points clearly show this difference. Some CBs however cease their equilibrium existence before reaching H_{cr} , which indicates instabilities before the critical point. Here it should be noted that there is a difference between unstable (H_u) and critical

(H_{cr}) CB thicknesses. A given CB can reach its existence limit (H_{cr}), only if it is stable over the entire definition region, i.e. only if there are no $H_u < H_{\text{cr}}$. The most simple case illustrating the difference between H_u and H_{cr} is the capillary cylinder ($\theta = 90^\circ$). Such capillary shape virtually could be stretched unlimitedly, i.e. $H_{\text{cr}} \rightarrow \infty$. However, it has been shown over ca. 140 years ago [20], that this shape is stable only up to $H_u \approx 0.66R$. Of course, the critical point can only be experimentally studied if the CB is stable since we do not have any available data for H_u , from our experiments, we have compared the observed transition parameters with numerical data for H_{cr} . On the other hand, as shall be shown (Appendix B), there is not much difference in where this transition originates, be it around H_u or H_{cr} , because for both cases the same mechanism (linear perturbation) is presumed.

Very indicative for a concave CB behaviour is the dependence of its azimuthal ($1/r_m$) and meridional (K) curvatures in the neck

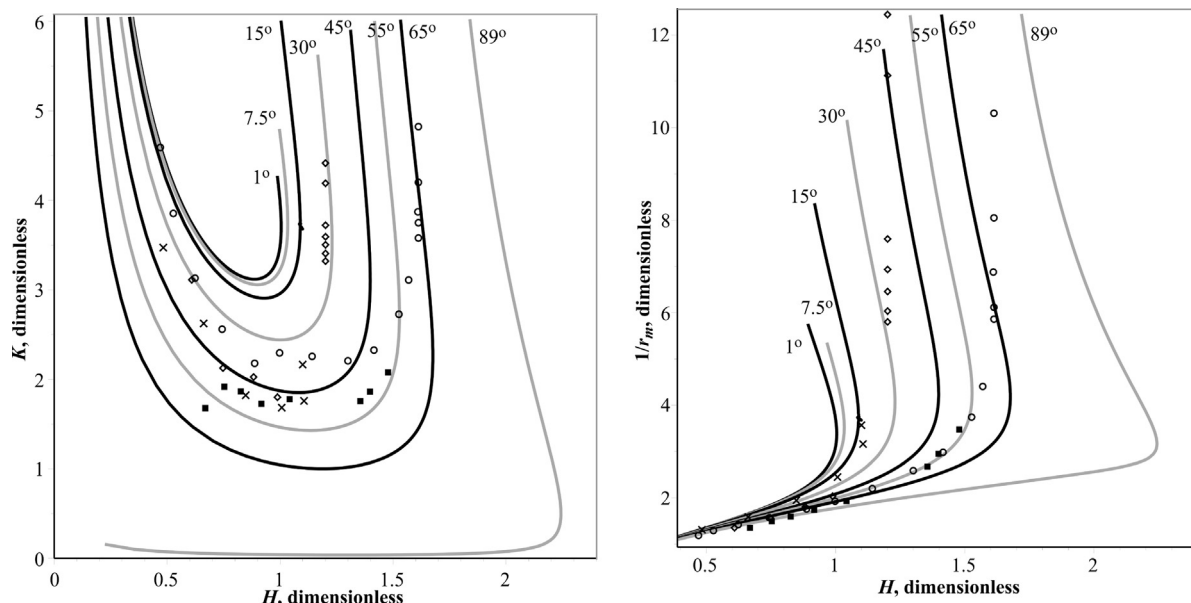


Fig. 6. Diagram of the meridional (left) and azimuthal (right) curvatures vs. bridge thickness for concave bridges. Solid lines—*theoretical isogons*; circle—*experimental data for IL_1*; box, solid box and solid circle—*experimental data for water*; diamond—*experimental data for IL_6*; diagonal cross—*experimental data for IL_5*.

as a function of the thickness, H (Fig. 6). Here again the existence of extrema at $H=H_{\text{cr}}$ is observed, dividing the respective isogons to thermodynamic and non-thermodynamic branches, similar to $H(R)$ (Fig. 5). Note that the extremal (critical) thicknesses H_{cr} of both Figs. 5 and 6 coincide. Concerning the distribution of the experimental points, there is one significant difference between Figs. 5 and 6. The data corresponding to the equilibrium states lie on the same thermodynamic branches ($0 \leq H \leq H_{\text{cr}}$) for all three diagrams ($H(R)$, $r_m^{-1}(H)$, $K(H)$), but in Fig. 6 additional post-critical values (the vertical series of points at H_{cr}) are observed. The reason for this is that at H_{cr} all geometrical parameters, except for the two neck curvatures which change significantly, take constant value. This is also an experimental proof for the local character of the observed instabilities.

3.2. Hydrodynamic states

As already noted, at thicknesses $H \geq H_{\text{cr}}$, a certain liquid bridge, given that it is stable to that point, passes in a non-equilibrium (hydrodynamic) state. Here we will shortly analyse this state and propose a model for it. Details can be found in Appendix B, while here only the most expressive results will be presented and compared with experimental data. Distinctive for the hydrodynamic regime is that the active zone is localized in the narrow neck region. This is best shown by comparing parameters in the different CB regions. Thus, for instance, the contact parameters, measured far from the active zone (radius, R and angle, θ), remain practically constant as the hydrodynamic regime progresses. The parameters which undergo the most substantial change are the two curvatures (azimuthal and meridional) in the neck region (Fig. 6). Instructive for the modelling is the analogy between the process of thinning in concave CB and the dynamics of microscopic thin foam films [e.g. [25]]. In Fig. 7 two states are sketched: quasi-static and hydrodynamic for the mentioned systems. With the classical method from the 60s [26], the soap film is formed from a double concave droplet in the capillary tube via sucking out the liquid. Given that the distance between the menisci is large enough, the system is in a mechanical equilibrium (quasi-static states). This situation corresponds to a small stretching of CB (far from the critical point). Brought closer than a certain thickness of the double concave droplet gap, the quasi-static state is disturbed, the menisci deform and a thin film is formed, which spontaneously thins out further.

The soap film thinning corresponds to the CB hydrodynamic regime. The driving force of both systems is proportional to the capillary pressures difference in the deformed active zone and non-deformed parts of meniscus. Along with the similarities, there are substantial differences in soap film and CB equilibrium states. So for instance, during the thinning, the soap film radius practically remains constant (changing only its thickness). With CB, change is observed in both curvature radii. The neck radius decreases, i.e. the azimuthal curvature ($1/r_m$) increases, while at the same time the meridional curvature (K) shows more complex behaviour (Fig. 6). According to the classical linear response theory [27,28], kinetics near the critical point is governed by the relation $\partial_t \zeta_k = \beta_k \zeta_k$, where ζ_k is the k th Fourier component of the deformation and $\partial_t \zeta_k$ is its velocity (details in Appendix B). Generally the time constant β_k (eigen value) is a complex quantity, but as shown in Appendix B, in our case it has only a real part. An important indication for the stability is the sign of β_k . At $\beta_k > 0$ the ζ_k components grow, i.e. the system is unstable and vice versa. In the continuum media, the time constant depends on the wave number k , i.e. $\beta_k(k)$ (often named in the literature as dispersion relation [29]). Most interesting are systems for which the coefficient β_k can be both positive and negative. The value $k=k_u$, for which β_k nullify, $\beta_k(k_u)=0$, divide the wave spectrum to stable ($k_u < k$) and unstable ($k_u > k$). For instance, for a concave bridge we have derived $\beta_k = \beta_0(k_u^2 - \bar{k}^2)\bar{k}^2$,

where $\beta_0 = \sigma/16\mu r_m$, $\bar{k} = kr_m \bar{k}_i^2 = 1 + (Kr_m)^2$, Eq. (B.5). It is important to note that the particular expression for β_0 is result of the "lubrication approximation", i.e. it is valid in the case of concave bridges (see Appendix B). It is easily seen that $\beta_k(k)$ is in maximum at $\bar{k}^2 = \bar{k}_u^2/2$, $\beta_{\max} = \beta_0 \bar{k}_u^4/4$, the value of which will be used further for comparison with the experimental data. In Fig. 8 is given the phase diagram V_m vs. $(r_c - r_m)$ (recalculated from the primary $r_m(t)$ data) of hydrodynamic regime for concave CB. In the framework of the acquired model (linear instability, see Appendix B) this relation is linear, $V_m = \beta_{\max}(r_c - r_m)$ with slope β_{\max} . The fitting line passes satisfactorily through the experimental points, but more important is that its slope corresponds to the theoretical evaluation, $\beta_{\max} \approx \beta_0 \approx 10^3 \text{ s}^{-1}$. This order of magnitude is obtained using the RTIL physical parameters and the value for $r_c \approx 10^{-4} [\text{m}]$ (see Table 1 and Fig. 8).

4. Conclusion

Subject of the present work are the observed processes in the vicinity (shortly before and after) of the CB critical state. The experiments have shown that this equilibrium state, is unstable, followed by a hydrodynamic process and CB breakage at the end. Characteristic is that all dynamic changes of concave CB take place in the narrow neck region, by analogy with the micro foam films dynamics. The proposed model based on the lubrication approximation enables a good explanation of the experimental data, in some cases even their satisfactory quantitative estimations. Nevertheless, critical point processes deserve additional investigations. So for instance, breakage capturing with a higher class camera and an adequate modelling of the process are necessary.

Appendix A.

Here follow a brief derivation and analysis of some CB equilibrium aspects. We are going to consider bridges between parallel solid identical plates, i.e. axisymmetric bridges (circular TPC), equal contact angles ($\theta_+ = \theta_- \equiv \theta$) and contact radii ($R_+ = R_- \equiv R$) on the upper/lower plate. The condition for mechanical equilibrium is $P_\sigma = \Delta P$, where P_σ is the capillary pressure and $\Delta P = P_i - P_e$ is the pressure difference at both sides of the capillary surface. Because of the axial symmetry, the capillary pressure can be written as [1]:

$$P_\sigma = \frac{\sigma}{r} \frac{dr \sin\varphi}{dr} = \Delta P, \quad (\text{A.1})$$

where r and φ are current coordinates. In this symmetry, the separate curvatures are defined as follows: $1/r_m = \sin\varphi/r$ (the so-called azimuthal curvature); $K = dsin\varphi/dr$ (meridional curvature). The angle φ is defined between the normal vector at a given point of the generatrix and the vertical axis z (see Fig. A1).

The first integral of the pressure balance Eq. (A.1) (in scaled form) offers no difficulty and using the boundary condition $\varphi(r=r_m) = 90^\circ$, one obtains

$$x \sin\varphi = C(x^2 - 1) + 1 \quad (\text{A.2})$$

with $x \equiv r/r_m$ and $C \equiv \Delta P r_m/2\sigma$ respectively. Applying Eq. (A.2) to the contact ($x=X$) one obtains:

$$C = \frac{X \sin\theta - 1}{X^2 - 1}, \quad (\text{A.3})$$

where $X \equiv R/r_m$. Relation (A.3) clearly shows the algebraic character of C , i.e. the algebraic character of the capillary pressure P_σ . It can be positive, zero or negative. At convex generatrix ($X < 1$), in the entire interval of angles ($\pi/2 < \theta \leq \pi$), the capillary pressure is positive ($C > 0$). In the case of concave generatrix ($1 \leq X \leq X(H_{\text{cr}})$, $0 \leq \theta < \pi/2$) the sign of C depends on the value of $X \sin\theta$. For instance,

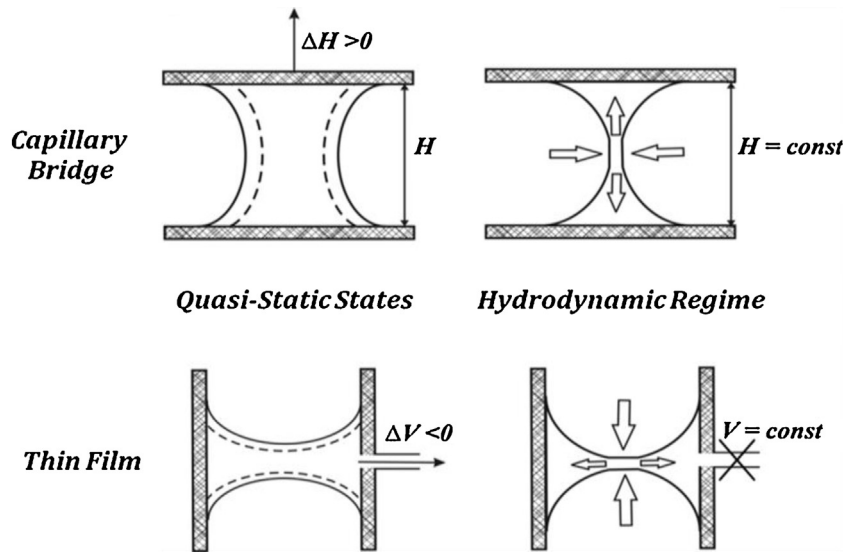


Fig. 7. Sketches of static and dynamic states of CBs and soap films.

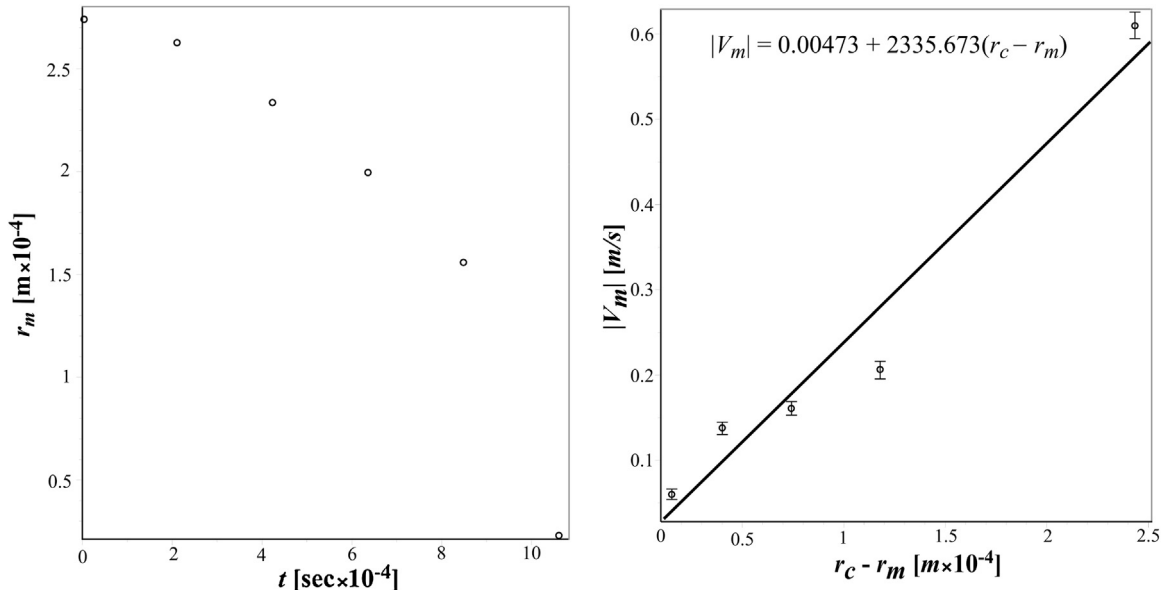


Fig. 8. Experimental validation of proposed model. Left—experimental data r_m vs. t ; right—phase diagram $|V_m|$ vs. $(r_c - r_m)$.

at $X \sin \theta < 1, C < 0$ (negative capillary pressure); at $X \sin \theta = 1, C = 0$ and we have a catenoidal state.

The complete analysis of CB behaviour requires integration of Eq. (A.2). In essence, this integration yields the generatrix equation $z(x, C)$, which in our notations can be presented as:

$$y(x, C) = \frac{R I_0(x, C)}{X}, \text{ with } I_0(x, C) = \pm \int_1^x \frac{1 + C(\xi^2 - 1)}{\sqrt{\xi^2 - [1 + C(\xi^2 - 1)]^2}} d\xi \quad (\text{A.4})$$

with $y \equiv z/r_m$. The integral $I_0(x, C)$ describes the upper part of the generatrix curve (above the equator, $y > 0$, see Fig. A1). It is sign ‘±’ determines whether the CB is concave (positive sign, $X > 1$, $0 \leq \theta < \pi/2$) or convex (negative sign, $X < 1$, $\pi/2 < \theta \leq \pi$). Traditionally I_0 is presented via (Legendre's) elliptic integrals first and second kind F, E , [2], but here we use direct numerical calculation via a Fehlberg fourth-fifth order Runge-Kutta method with a degree four

interpolator [30–32]. The experimentally determinable parameter related to I_0 is the CB height H :

$$H^*(X, C) = \frac{2R^* I_0(X, C)}{X} \quad (\text{A.5})$$

here all dimensionless parameters are already scaled by the cube root of the CB volume $V^{1/3}$, ($y^* = z(x, C)/V^{1/3}$, $H^* = y^*(X, C)$, $R^* = R/V^{1/3}$). This scaling transforms the dimensionless expression for the volume into a relation, similar to Eq. (A.5):

$$1 = \frac{2\pi(R^*)^3 I_2(X, C)}{X^3} \quad (\text{A.6})$$

where

$$I_2(X, C) = \pm \int_1^X \xi^2 \frac{1 + C(\xi^2 - 1)}{\sqrt{\xi^2 - [1 + C(\xi^2 - 1)]^2}} d\xi \quad (\text{A.7})$$

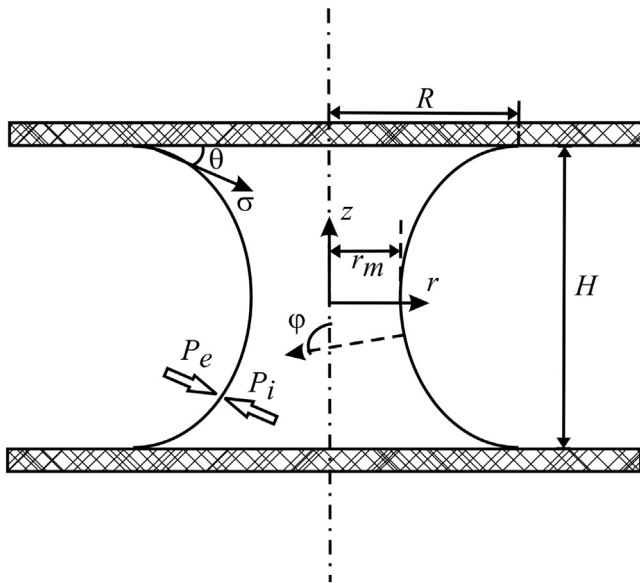


Fig. A1. Sketch of a concave CB with added mechanical and geometric parameters.

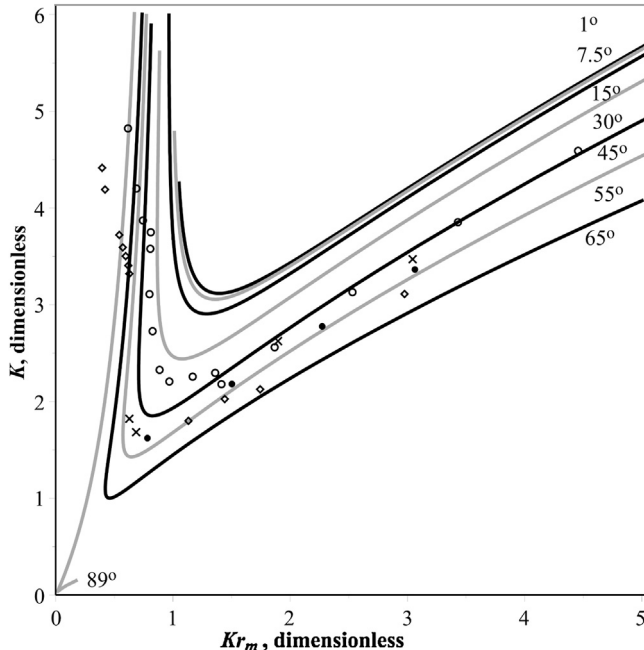


Fig. B1. Meridional curvature, K vs. the ratio of the two neck curvatures Kr_m . Solid lines—*theoretical isogones*; circle—*experimental data for IL-1*; box, solid box and solid circle—*experimental data for water*; diamond—*experimental data for IL-6*; diagonal cross—*experimental data for IL-5*. The hydrodynamic regime begins beyond the minima (critical points).

The theoretical values of curvatures r_m^{-1} and K in the neck are calculated via Eqs. (A.6) and (A.3):

$$r_m^{-1} = \sqrt[3]{\frac{1}{2\pi I_2(X, C)}}; K = (1 - 2C)r_m^{-1} \quad (\text{A.8})$$

Appendix B.

For the considered CB hydrodynamic regime in the active zone the so-called lubrication approximation is assumed, evidence for which is the experimental fact that the hydrodynamic interactions begin in the region $Kr_m \leq 1$ (Fig. B1).

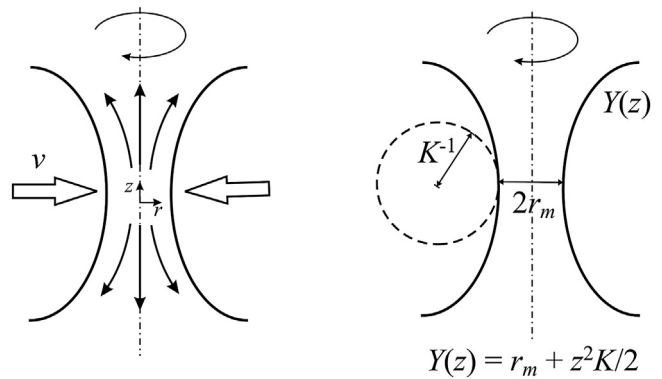


Fig. B2. Sketches of the neck (active) zone: left—the velocity field with v as the velocity of neck thinning; right—the parabolic approximation parameters.

Supposing the details of the lubrication approximation derivation, validity etc. are known, [see e.g. in Ref. [25]] we are using here its final form:

$$\text{a)} \mu \frac{1}{r} \frac{\partial}{\partial r} r \frac{\partial v_z}{\partial r} = \frac{dp}{dz}; \text{ b)} \frac{1}{r} \frac{\partial}{\partial r} (rv_r) + \frac{\partial v_z}{\partial z} = 0, \quad (\text{B.1})$$

where v_r, v_z are the fluid velocity components, p the dynamic pressure and μ the dynamic viscosity. Here we will point out that Eq. (B.1) is the same as this one in the classical problem of flow through a pipe (Poiseuille flow [33]). After the integration of Eq. (B.1) one gets,

$$4\mu v_z = -\frac{dp}{dz}(Y^2 - r^2), \quad (\text{B.2})$$

where $Y(z) = r_m + z^2 K/2$ is the generatrix equation in the neck vicinity (parabolic approximation), with K as the neck generatrix curvature (Fig. 4). The used boundary condition $v_z(r = R) = 0$ is equivalent to tangentially immobile (blocked) bridge interfaces. Mobility of liquid surfaces is a function of the so-called Marangoni effect, more about which can be found in e.g. in Ref. [25]. The combination of Eqs. (B.2) and (B.1) after integration gives,

$$16\mu V_r = Y^3 \frac{\partial^2 p}{\partial z^2} + 4Y^2 \frac{\partial p}{\partial z} \frac{\partial Y}{\partial z}. \quad (\text{B.3})$$

where $V_r = v_r(r = Y) = \partial Y / \partial t$. The result (B.3) is a non-linear equation, the solution of which needs special analysis, which is beyond the scope of the current study. Here will suffice an analysis at the point ($z = 0$), where $\partial Y / \partial z = 0, Y = r_m$. Accounting the definition of the perturbation ζ (see below), the velocity $V_r(z = 0) = \partial r_m / \partial t$ is related to the deformation velocity as $\partial r_m / \partial t = -\partial \zeta / \partial t$. Thus Eq. (B.3) is reduced to,

$$-16\mu \frac{\partial \zeta}{\partial t} = r_c^3 \frac{\partial^2 p}{\partial z^2}. \quad (\text{B.4})$$

As already mentioned, the process is driven by capillary forces caused by the deformation ζ of equilibrium generatrix. Denoting the (equilibrium) neck radius in the critical (non-perturbed) state as r_c , the deformation $\zeta(t, \dots)$ can be presented as $\zeta = r_c - r_m$ (Fig. B3). The pressure p in (B.3) can be presented, similar to the other parameters in the form $p(\zeta) = p_c + \delta p$, where $p_c = \sigma(1/r_c - K_c) = \text{const}$ is the equilibrium capillary pressure in the critical point and δp is its perturbation. In the scope of the linear perturbation theory, $\delta p \sim \zeta$, which for the azimuthal curvature component perturbation directly follows from the difference $1/(r_c - \zeta) - 1/r_c \approx \zeta/r_c^2$. More complicated is the problem with the perturbation of K . This is because the curvature of the non-perturbed surface K influences on the perturbation curvature δK (Fig B2).

This is a differential geometry problem, the solution of which in our case reads $K(\zeta) = K_c + (\zeta'' e; e; + K_c^2 \zeta)$, with $\zeta'' \equiv \partial^2 \zeta / \partial z^2$. For

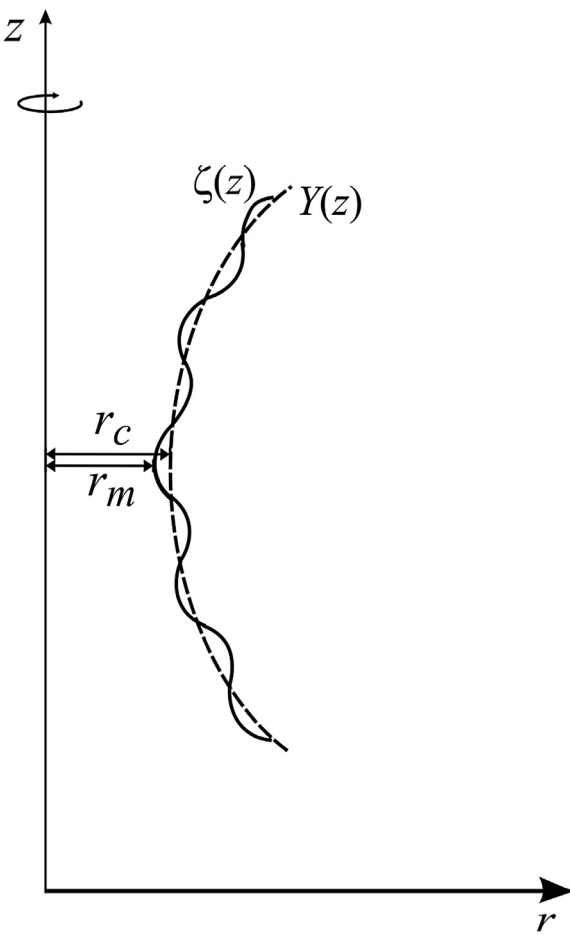


Fig. B3. Sketch of a perturbed generatrix (the solid line); dashed line—the unperturbed generatrix.

those interested in the matter we recommend mathematical manuals, encyclopaedias, etc. (see e.g. in Ref. [34]). Having in mind the linear nature of the perturbation ζ , it can be presented in Fourier series with $\zeta_k = A_k \exp(\beta_k t + izk)$, where A_k , β_k are well-known parameters of the k th component. Following this train of thought, for the k th component of curvature perturbation, δK_k it can be written, $\delta K(\zeta_k) = (K_c^2 - k^2)\zeta_k$ and for the pressure perturbation δp_k , respectively,

$$\delta p_k = \sigma(1/r_c^2 + K_c^2 - k^2)\zeta_k \quad (\text{B.5})$$

After inserting Eq. (B.5) in Eq. (B.6), one obtains the so-called dispersion condition,

$$\beta_k = \beta_0(1 + K_c^2 r_c^2 - k^2 r_c^2) k^2 r_c^2, \quad (\text{B.6})$$

with $\beta_0 = \sigma/16\mu r_c$ as the considered process characteristic time constant.

According to the theory [e.g. [35]], the instability kinetics is determined by the fastest wave, i.e. by the wave with maximal β . In particular from Eq. (B.5) it follows, $\beta_{\max} = \beta_0(1 + K_c^2 r_c^2)^2/4$.

References

- [1] N.M. Princen, The Equilibrium Shape of Interfaces, Drops and Bubbles. Rigid and Deformable Particles at Interfaces, in Surface and Colloid Science, in: E. Matijevich (Ed.), Wiley-Interscience, New York, 1969.
- [2] P. Kralchevsky, K. Nagayama, Particles at Fluid Interfaces and Membranes, Elsevier, Amsterdam, 2001.
- [3] A.D. Myshkis, V.G. Babskii, Low-Gravity Fluid Mechanics: Mathematical Theory of Capillary Phenomena, Springer-Verlag, 1987.
- [4] O.V. Voinov, Hydrodynamics of wetting, Fluid Dyn. 11 (1976) 714–721.
- [5] R.G. Cox, J. Fluid Mech. 168 (1986) 169–194.
- [6] R.G. Cox, J. Fluid Mech. 168 (1986) 195–220.
- [7] O.I. Vinogradova, Int. J. Miner. Process. 56 (1999) 31.
- [8] T.D. Blake, J.M. Haynes, J. Colloid Int. Sci. 30 (1969) 421–423.
- [9] H. Eyring, in: The Theory of Rate Processes: The Kinetics of Chemical Reactions, Viscosity, Diffusion and Electrochemical Phenomena, McGraw-Hill, New York, 1941.
- [10] R.D. Deegan, O. Balmajin, T.F. Dupont, S.R. Nagel, T.A. Witten, Capillary flow as the cause of ring stains from dried liquid drops, Nature 389 (1997) 827–829.
- [11] R.D. Deegan, O. Balmajin, T.F. Dupont, S.R. Nagel, T.A. Witten, Contact line deposits in an evaporating drop, Phys. Rev. E 62 (2000) 756–765.
- [12] Hua Hu, G.L. Ronald, Analysis of the effects of marangoni stresses on microflow in an evaporating sessile droplet, Langmuir 21 (2005) 3972–3980.
- [13] V.M. Starov, M.C. Velarde, C. Radke, in: J. Wetting and Spreading Dynamics. Surfactant Sci. Series, vol. 138, CRC Press, 2007.
- [14] T. Vogel, Stability of a liquid drop trapped between two parallel plates, SIAM: J. Appl. Math. 47 (3) (1987) 516–525.
- [15] I. Martinez, J.M. Perales, Experimental analysis of the breakage of a liquid bridge under microgravity conditions, Adv. Space Res. 48 (2011) 465–471.
- [16] P.V. Petkov, B.P. Radoev, Statics and dynamics of capillary bridges, Colloids Surf. A: Physicochem. Eng. Aspects 460 (20) (2014) 18–27.
- [17] R. Osserman, A Survey of Minimal Surfaces, Dover, New York, 1986.
- [18] K.G. Marinova, S. Tcholakova, N.D. Denkov, Hydrophobization of glass surface by adsorption of polydimethylsiloxane (PDMS), Langmuir 21 (2005) 11729–11737.
- [19] I.T. Ivanov, R.I. Slavchov, et. al., Ann. Univ. Sofia Fac Chim. 102/103 (2005) 259–271.
- [20] F.W. Pierson, S. Whitaker, J. Colloid Interface Sci. 54 (2) (1976) 219–230.
- [21] Lord Rayleigh, On the instability of liquid jets, Proc. Math. Soc. 10 (1878) 4–13.
- [22] A. Nelson, Rayleigh Instability of an Annulus, 2000: http://willson.cm.utexas.edu/Research/Sub_Files/Surface_Phenomena/Spring%202000/Rayleigh_Instability_of_an_Annulus.pdf.
- [23] B. Radoev, P. Petkov, I.T. Ivanov, Capillary Bridge: A Tool for Investigating Contact Angle in Surface Energy, Intech, Rijeka, 2015, <http://dx.doi.org/10.5772/60684>, ISBN 978-953-51-2216-6.
- [24] M. Ito, T. Sato, In situ observation of a soap-film catenoid: a simple educational physics experiment, Eur. J. Phys. 31 (2) (2010) 357–365.
- [25] B. Radoev, D. Dimitrov, I.B. Ivanov, Colloid Polym. Sci. 252 (1974) 50–55.
- [26] A. Scheludko, Adv. Colloid Interface Sci. 1 (1967) 391–464.
- [27] W. Hove, Ph.D. Dissertation, Friendlich-Wilhelms, Universitat zu Berlin, 1887.
- [28] B. Radoev, A. Scheludko, E. Manev, Critical thickness of thin liquid films, J. Colloid Interface Sci. 95 (1) (1983) 254–265.
- [29] M.J. Lighthill, Waves in Fluids, University Press, Cambridge, 1978.
- [30] E. Fehlberg, Klassische Runge–Kutta-formeln vierter und niedrigerer ordnung mit schrittweiten-kontrolle und ihre anwendung auf Waermeleitungsprobleme, Computing 6 (1970) 61–71.
- [31] G.E. Forsythe, M.A. Malcolm, C.B. Moler, Computer Methods for Mathematical Computations, Prentice Hall, New Jersey, 1977.
- [32] W.H. Enright, K.R. Jackson, S.P. Norsett, P.G. Thomsen, Interpolants for Runge–Kutta formulas, ACM TOMS 12 (1986) 193–218.
- [33] C.O. Bennett, J.E. Myers, Momentum, Heat, and Mass Transfer, McGraw-Hill, 1962, 2016.
- [34] G. Korn, Th. Korn, Mathematical Handbook, Dover Publications Inc., Mineola, NY, 2000.
- [35] A. Vrij, Discuss. Faraday Soc. 42 (1966) 23–33.

Glossary

- C: Dimensionless capillary pressure
- H: Bridge thickness
- H_c : Critical bridge thickness
- H_u : Point of instability
- K: Meridional neck curvature
- $P_{i/e}$: Internal/external pressure
- P_c : Capillary pressure
- R: Contact radius
- V: Capillary bridge volume
- V_r : Generatrix velocity in the neck of the bridge
- X: Dimensionless radius
- R/r_m , k : Wave number
- k_u : Unstable wave number
- r_c : Critical neck radius
- r_m : Capillary bridge neck radius
- β_0 : Relaxation time
- β_k : Time constant
- θ : Contact angle
- μ : Viscosity
- ρ : Density
- σ : Surface tension